

Direct Measurement of Coating Thermal Noise in Optical Resonators

S. Gras and M. Evans

*Massachusetts Institute of Technology, 185 Albany St. NW22-295, 02139 MA, USA**

(Dated: December 3, 2024)

The best measurements of space and time currently possible (e.g. gravitational wave detectors and optical reference cavities) rely on optical resonators, and are ultimately limited by thermally induced fluctuations in the reflective coatings which form the resonator. We present measurements of coating thermal noise in the audio band and show that for a standard ion beam sputtered coating, the power spectrum of the noise does *not* have the expected power-law behavior.

PACS numbers: 04.80.Nn, 06.30.-k, 05.40.Jc, 07.60.-j

I. INTRODUCTION

High-reflectivity mirrors play an important role in precision optical experiments such as gravitational-wave detectors [1, 2], the best frequency references [3, 4], and macroscopic quantum measurements [5, 6]. These mirrors depend on multilayer coatings which are deposited with either physical methods (sputtering, pulse laser deposition, molecular beam epitaxy) or chemical methods (vapor deposition). While the coating is critical to the optical measurement, Brownian motion in coatings can present a limiting noise source due to nonzero mechanical dissipation in the deposited layers.

Ion beam sputtering (IBS) for amorphous coatings and molecular beam epitaxy for crystalline coatings currently produce the lowest mechanical loss [7]. Research into deposition parameters and materials which result in high-quality optical coatings with good optical properties (high coating uniformity, low optical absorption, and low scatter loss) and low thermal noise is on-going since lowering coating thermal noise (CTN) would provide substantial improvement for many experiments (e.g., future gravitational-wave detectors [8–10]).

The CTN amplitude of new coating materials is most frequently obtained based on the measurement of the mechanical quality factors of the materials used in the coating. The techniques presented in the literature include, among others, suspended disks [11, 12], clamped cantilevers [13], and the gentle nodal suspension [14]. The level of CTN is then calculated from the measured parameters, such as mechanical loss angles, Poisson ratio, and Young’s modulus. However, due to uncertainties in the multilayer parameters the actual CTN may differ somewhat from the computed value and a direct measurement is necessary to accurately determine the CTN associated with a particular coating.

This paper describes a second application of a novel technique for the direct observation of the coating thermal noise, described in [15]. In short, this CTN measurement technique uses a single Fabry-Perot cavity, in which multiple transverse electromagnetic modes (TEM)

co-resonate: 00, 02 and 20. These modes probe different areas of the sample coating, and CTN appears as a fluctuation in the resonant frequencies of the two higher-order modes (see figure 1).

In Sec. II we describe analytical calculations of the coating thermal noise for the fundamental and higher-order modes in the linear and folded cavities. Sec. III describes our experimental setup. In Sec. IV we explain how to extrapolate CTN measured with higher-order modes to the fundamental mode. In Sec. V we present the measured CTN of multiple samples, and discuss the implications of this result for Advanced LIGO [16].

II. COATING THERMAL NOISE

The fluctuation-dissipation theorem [17] connects the properties of an observable, in our case the position of a mirror surface, with the dissipation of mechanical energy. The single-sided power spectral density (PSD) of the observable is given by

$$S_x(f) = \frac{2k_B T}{\pi^2 f^2} \frac{W_{\text{diss}}(f)}{F_0^2}, \quad (1)$$

where T is the temperature, k_B the Boltzmann constant, and W_{diss} is the time averaged dissipated power when the mirror is subjected to a sinusoidally varying force $F(t) = F_0 \cos(2\pi ft)$ [18]. Though there are many dissipation mechanisms in a coating which can cause the observable to fluctuate [2, 19], here we focus on the dominant mechanism: mechanical loss in the coating.

We start by considering a simplified model of the coating as a single lossy layer of thickness d . (Real coatings are the stacks of alternate layers with low/high refractive index material.) The power dissipation in single layer can be written as

$$W_{\text{diss}}(f) = \frac{2F_0^2 d(1 + \sigma)(1 - 2\sigma)\phi}{\omega_S^2 Y} \times f, \quad (2)$$

where ω_S is the beam size, while σ , Y and ϕ are the Poisson ratio, Young’s modulus and mechanical loss angle of the composite coating material. By combining Eqns. 1 and 2 we expect a $1/f$ dependence of the PSD of CTN,

* sgras@ligo.mit.edu

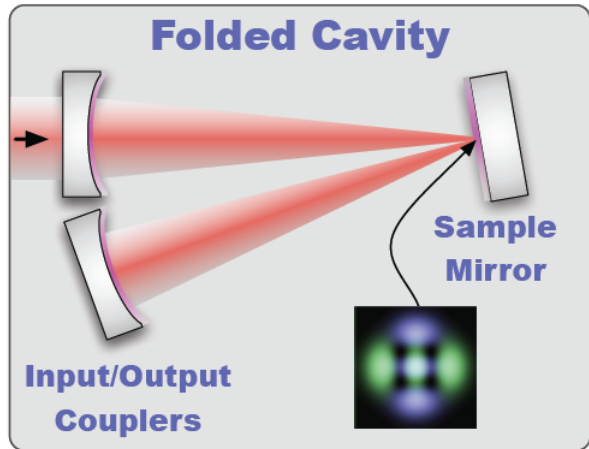


FIG. 1. At the heart of this experiment is a small, high finesse cavity, with a folding mirror (the sample to be measured) equidistant from the input and output mirrors. The inset image shows the TEM20 and TEM02 modes used to make the coating thermal noise measurement. Since these modes overlap only in a small central area, noise in the coating causes changes in the difference between their resonant frequencies, while most other noises sources cancel in this difference.

assuming that ϕ and other mechanical properties are frequency independent [20]. To facilitate comparison with previous results we present our measurements as amplitude spectral densities (ASD) with units of $\text{m}/\sqrt{\text{Hz}}$, i.e. $N_x(f) = \sqrt{S_x(f)}$.

III. EXPERIMENTAL SETUP

The experimental setup used to obtain the data presented in this paper has evolved significantly since the previous publication [15]. This section briefly describes the setup, the redesigned readout and control system, and the dominant noise sources in the experiment.

A. Optical Cavity

At the core of the experiment is a 3-mirror folded cavity, with the sample to be measured as the folding mirror (see Fig. 1). The cavity is placed on a vibration isolation platform and is in vacuum at a pressure of 10^{-5} Torr. This folded configuration is ideal for rapid testing of high reflectivity coatings, and is compatible with the witness flats commonly included in the coating fabrication process of large optics.

The cavity is nearly concentric, with a total length of $L = 99.5$ mm and input and output couplers with radius of curvature $R = 50.7$ mm. This produces a small waist size ω_0 near the sample mirror, and a transverse mode spacing f_{TMS} easily accessible by radio frequency (RF)

TABLE I. Measured cavity parameters during collection of the data.

Parameter	Symbol	TEM02	TEM20
Intra-cavity power, W	P_{circ}	2	2
Transmitted power, mW	P_{tr}	0.4	0.4
Cavity pole, kHz	ν_{cav}	50.8	50.0
Finesse	\mathcal{F}	15.06 k	15.30 k
Round trip loss, ppm	l	17	11
Mode frequency, MHz	$2 \times f_{\text{TMS}}$	276 ± 2	280 ± 2
Beam size, μm	ω_S	54	54
RoC (effective), mm	R	50.7	50.8
Laser wavelength, nm	λ	1064	
Cavity length, mm	L	$L_1 + L_2 = 46.45 + 53.07$	
Folding angle, deg	α	17.23	

acousto-optic modulators (AOMs) of

$$\omega_0 = \sqrt{\frac{\lambda \sqrt{\epsilon L/2}}{\pi}} \simeq 49 \mu\text{m} \quad (3)$$

$$f_{\text{TMS}} = \frac{c}{\pi L} \sqrt{\frac{\epsilon}{R}} \simeq 133 \text{ MHz},$$

where $\epsilon = R - L/2 \simeq 1$ mm, $\lambda = 1064$ nm is the laser wavelength, and c is the speed of light [21].

This value of f_{TMS} implies that the frequency difference between TEM00 and TEM02 or TEM20 is 288 MHz if the modes are in the same polarization. In practice, the horizontal and vertical radii of curvature are slightly different, and resonant frequencies of the TEM02 and TEM20 modes are separated by a few MHz.

B. Control Scheme

The control scheme has been simplified with respect to that shown in our previous publication (see figure 2). The primary change is the move from modulated readout for controlling the higher-order-modes to a simple unmodulated or DC readout. This method requires holding the cavity off resonance such that the power in transmission is given by

$$P_T(\delta) = P_{\text{max}} \frac{1}{1 + \delta^2} \quad (4)$$

where P_{max} is the transmitted power on-resonance (i.e., at the peak of the Lorentzian profile) and δ is the detuning from resonance normalized by the cavity pole frequency (ν_{cav} , see Table I).

The slope of the fringe provides a frequency discriminator which can be used as an error signal for control by subtracting a fixed offset value $\Delta_0 = P_T(\delta_0)/P_{\text{max}}$. The detuning δ_0 for any particular offset can be found by inverting Eqn.4, and the corresponding normalized dis-

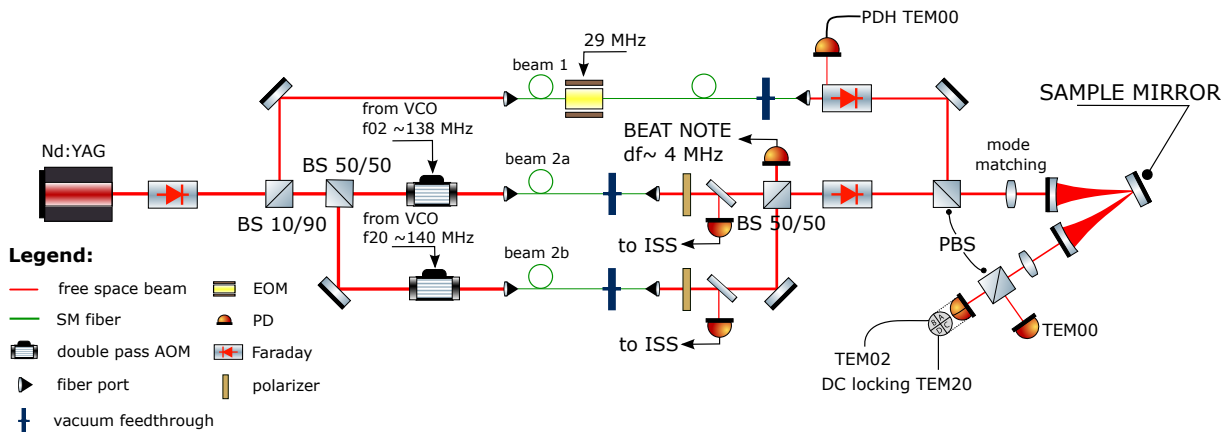


FIG. 2. The experimental setup for the multi-mode measurement involves a Nd:YAG laser (far left) and an in-vacuum high-finesse cavity (far right). In order to avoid multiple lasers, and the multiple sources of frequency and intensity noise they would introduce, a single laser beam is split into 3 paths, 2 of which are shifted in frequency (with AOMs). The laser frequency is controlled to lock the TEM00 mode to the cavity length with PDH locking scheme while the TEM02 and TEM20 modes are DC locked to the cavity by controlling their frequency differences with respect to the laser frequency. Beams 2a and 2b before entering the cavity are intensity stabilized by actuating RF power on AOMs using Intensity Stabilization Servo (ISS) loops. The primary output of the experiment is the difference between the TEM02 and TEM20 resonant frequencies (labeled BEAT NOTE), changes which are dominated by the coating thermal noise of the sample. Note, beams 1, 2a, 2b are the fundamental TEM00 modes. A conversion of beams 2a, 2b into TEM02 and TEM20 takes place in the cavity.

criminator magnitude is given by

$$D_{T0} = \frac{1}{P_{\max}} \left| \frac{\partial P_T}{\partial \delta} \right|_{\delta_0} = \frac{2\delta_0}{(1 + \delta_0^2)^2} \quad (5)$$

The maximum value of the discriminator corresponds to $\delta_0 = \sqrt{3}/3$, where $\Delta_0 = 0.75$. This corresponds to the highest signal to noise ratio operating point for regions in which readout noise dominated (see Sec. III C 1). However, the measurement is also limited by shot noise (see Sec. III C 2) for which the highest signal to noise ratio can be achieved by maximizing $D_{T0}/\sqrt{P_T}$, which requires $\delta_0 = \sqrt{2}/2$ and $\Delta_0 = 0.67$. While our measurement is not limited by relative intensity noise (RIN), it is useful as a limiting case to note that the optimal offset for a RIN-limited measurement maximizes D_{T0}/P_T , which requires $\delta_0 = 1$ and $\Delta_0 = 0.5$.

Since our measurements are mainly limited by a mixture of shot noise and readout noise, we set the locking point to $\Delta_0 = 0.7$. That is, we operate with the cavity detuned such that transmitted power is 70% of the on-resonance value.

C. Noise sources

The measured ASD noise $N_{02/20}$ contains the coating thermal noise N_{CTN} as well as fundamental and technical noises. In this section we describe the major noise sources that contribute to $N_{02/20}$.

1. Oscillator Noise

The voltage controlled oscillator (VCO) used to measure the frequency difference between the higher order modes (see Fig. 3), has a noise level on the order of $N_{VCO} \sim 3 \text{ mHz}/\sqrt{\text{Hz}}$ below 1 kHz. Recall that this frequency difference is our primary output, since coating thermal noise of the sample mirror changes the resonance frequencies of these modes. VCO noise appear as

$$N_{02/20}^{VCO}(f) = \frac{\lambda L}{c} N_{VCO}(f) \sim 10^{-18} \frac{\text{m}}{\sqrt{\text{Hz}}}. \quad (6)$$

VCO noise has some frequency dependence, increasing by about a factor of 2 above 1 kHz, as shown in Fig. 3.

2. Shot noise

Photon counting noise, or “shot noise”, is an unavoidable noise source in precision optical measurements and sufficient power on the sensor is required to sustain the shot noise below the coating thermal noise level. The PSD of shot noise, normalized by the average photocurrent of the readout photodiode I_{pd} , is

$$S_{PD}^{\text{shot}} = \frac{2e}{I_{pd}} \quad (7)$$

where e is the electron charge. For a detection quantum efficiency η (probability that a photon arriving on the photodiode is converted to a free electron and measured as photo-current), this can be written as a relative

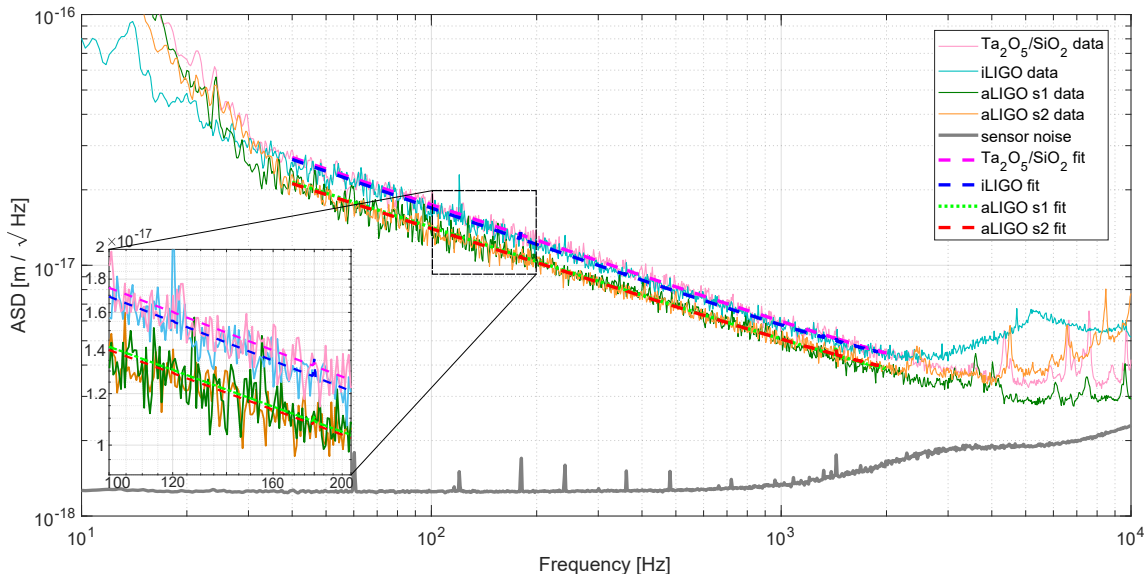


FIG. 3. The noise spectrum measured for 3 samples. Note that the plotted fit is the sum of CTN and the stationary noise contributions described in section III C. Non-stationary noise below 30 Hz from environmental vibrations and above 2 kHz from down-converted radio frequency (RF) interference, limit the extent of the fit.

intensity noise on transmission from the cavity

$$S_{\text{RIN}}^{\text{shot}} = \frac{2hc}{\eta\lambda P_{tr}} \quad (8)$$

where $P_{tr} \simeq 400 \mu\text{W}$ is the power on transmission and h is Planck's constant. Given the side-of-fringe locking described in section IIIB and equation 5, this results in a readout noise of

$$N_{02/20} = 0.7 \frac{\lambda}{\mathcal{F}} \times \sqrt{\frac{2hc}{\eta\lambda P_{tr}}} \sim 10^{-18} \frac{\text{m}}{\sqrt{\text{Hz}}} \quad (9)$$

which is comparable to the VCO noise described above.

3. Intensity noise

Side-of-fringe locking schemes like the one used in this experiment are vulnerable to intensity noise on the laser beam incident on the cavity. This is, in fact, the primary reason that the previous version of this experiment relied on a modulated readout scheme. We find, however, that intensity stabilization through feed-back, coupled with feed-forward noise cancelation, is sufficient to eliminate intensity noise in our readout below 10 kHz.

The pick-offs for our intensity stabilization servo (ISS) are in vacuum and sample the light incident on the cavity (see figure 2). The servo bandwidth is 40 kHz, and the residual intensity noise (mostly above 10 kHz) is removed from the transmitted light signal with a simple feed-forward circuit.

IV. EXTRAPOLATION TO TEM00 BEAMS

Any direct measurements of the CTN will be associated with a particular beam geometry, and it is often the case that the system of interest (e.g., a gravitational wave interferometer) has a different geometry. In order to predict the level of the CTN in the target system, extrapolation is necessary. The simplest example of this is for geometries which involve TEM00 Gaussian beams, such that the only difference is in the beam size, in which case the amplitude of CTN simply scales with beam radius.

Since the experiment described here measures the thermal noises sensed by TEM02 and TEM20 modes in a folded cavity (see Fig. 1), several other correction factors are necessary. To convert the CTN amplitude spectral density measured here, N_{CTN} , to CTN for a large TEM00 beam of size ω_L , we use

$$N_{\text{CTN}}^{00} = 0.616 \times \left(\frac{\omega_S}{\omega_L}\right) N_{\text{CTN}} \quad (10)$$

where ω_S is the beam size on the sample mirror (see Table I). A detailed description of our computation of the numerical correction factor can be found in [15].

V. EXPERIMENTAL RESULTS

This section describes the sensitivity of the experimental setup and results for four coating samples; a standard high-reflectivity coating, an initial LIGO coating sample, and two Advanced LIGO coating samples. All four coatings were produced by ion-beam sputtering.

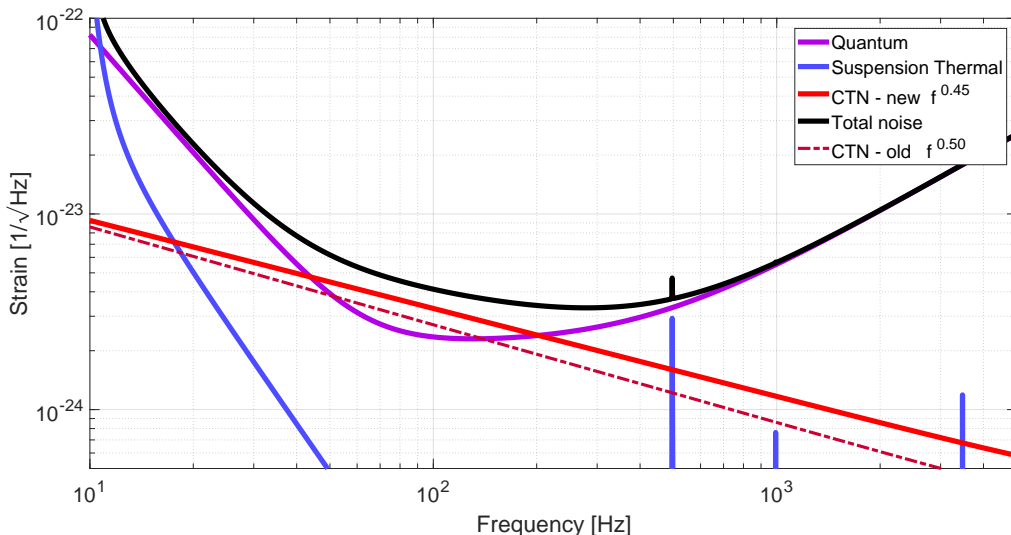


FIG. 4. The noise budget for aLIGO that incorporates a new measured value of the loss angle and the slope for coating thermal noise. A previous estimate of coating thermal noise ($\phi_{\text{SiO}_2} = 5.0 \times 10^{-4}$, $\phi_{\text{Ti}_2\text{O}_3} = 2.3 \times 10^{-4}$, slope index = 0.5) is included in the plot and marked as “CTN-old”. The new value of CTN results in 7% smaller detection range for binary neutron stars. For the quantum noise we assume the transmittance of signal recycling mirror to be $T = 33\%$. More information on the aLIGO sensitivity curve can be found in [22].

The standard coating was fabricated at 120°C using Argon as process gas. The deposition rate was 1.9 \AA/s for both SiO_2 and Ta_2O_5 . The sample was annealed at 450°C for 3 hours.

The initial LIGO and standard coating is stack of quarter-wave Ta_2O_5 - SiO_2 doublets while the Advanced LIGO coatings are complex multilayers consist of alternating layers of SiO_2 and Ta_2O_5 alloyed with 20% TiO_2 . All sample mirrors have a transmissivity less than 10 ppm at the measurement wavelength 1064 nm.

A. Coating Thermal Noise Power Spectrum

The measured amplitude spectral densities are shown in Fig. 3 and the folded cavity parameters are shown in Table I.

In our previous paper, we assumed a constant loss angle, and thus a $1/\sqrt{f}$ coating thermal noise ASD. With the increased sensitivity of the current experiment, we are able to measure CTN over a much broader frequency range (30 Hz - 2 kHz), which allows us to constrain this slope experimentally. We find that the best fit slope for all samples is near $f^{-0.45}$, which appears to match the frequency dependence of the loss angles found in [?].

The fitting of a series of spectra gives the following result for the coating thermal noise in our experiment:

$$N_{\text{CTN}}^{\text{aL}} = (14.0 \pm 0.2) \times 10^{-18} \left(\frac{100 \text{ Hz}}{f} \right)^{0.45 \pm 0.02} \frac{\text{m}}{\sqrt{\text{Hz}}}.$$

for our Advanced LIGO coating samples (see Fig. 3). Our fit is limited to the region above 30 Hz to avoid the

variable environmental noise at lower frequencies, and below 2 kHz to remain well above the readout noises and to avoid small noise peaks due down-converted radio frequency (RF) interference.

As expected, the other coating samples we measured have higher CTN, since they are simple SiO_2 and Ta_2O_5 quarter-wave stacks. The Initial LIGO coating sample has 19% higher CTN than the the Advanced LIGO coating:

$$N_{\text{CTN}}^{\text{IL}} = (16.7 \pm 0.1) \times 10^{-18} \left(\frac{100 \text{ Hz}}{f} \right)^{0.47 \pm 0.01} \frac{\text{m}}{\sqrt{\text{Hz}}}.$$

while the standard Ta_2O_5 - SiO_2 coating has 25% higher CTN than the Advanced LIGO coating:

$$N_{\text{CTN}}^{\text{Ta}} = (17.5 \pm 0.1) \times 10^{-18} \left(\frac{100 \text{ Hz}}{f} \right)^{0.47 \pm 0.03} \frac{\text{m}}{\sqrt{\text{Hz}}}.$$

These are consistent with a larger mechanical loss angle for Ta_2O_5 without TiO_2 .

B. Variation among aLIGO samples

The individual measurements of the two Advanced LIGO coating samples give the same slope, but slightly different values at 100 Hz ($N_{\text{CTN}}^{\text{S1}} = (13.9 \pm 0.1) \times 10^{-18}$ and $N_{\text{CTN}}^{\text{S2}} = (14.2 \pm 0.1) \times 10^{-18} \text{ m/Hz}^{1/2}$). Each sample was measured multiple times at several locations on the coating and the results were within the statistical error bars. The sample-to-sample variation of CTN, on the other hand, is statistically significant (about 3

σ) even though the magnitude of the difference is only 2%. The origin of this difference is not known to us, so we extend the uncertainty on our reported value of $N_{\text{CTN}} = (14.0 \pm 0.2) \times 10^{-18} \text{m/Hz}^{1/2}$ to include both measurements.

This value differs from our previous estimate $N'_{\text{CTN}} = (12.9 \pm 0.6) \times 10^{-18} \text{m/Hz}^{1/2}$ [15] by less than 2σ . The difference may be due in part to small systematic effect resulting from the new experimental set-up, or it may simply be due to statistics. Note that our previous measurement had a signal-to-noise ratio of 2 at 40 Hz (and less at other frequencies) and the fitting process assumed a white sensor noise, so systematic effects at the few percent level are not surprising.

C. Implications for Advanced LIGO

Extrapolation of our measured CTN to the CTN of a 6.2 cm beam on an Advanced LIGO end test mass (ETM) based on Eqn. 10 gives

$$N_{\text{CTN}}^{00}(100 \text{ Hz}) = (7.5 \pm 0.1) \times 10^{-21} \frac{\text{m}}{\sqrt{\text{Hz}}} \quad (11)$$

This is slightly higher than our previously reported value, and higher than the value used in Advanced LIGO design documents ($5.8 \times 10^{-21} \text{m}/\sqrt{\text{Hz}}$ at 100 Hz [23]). Accounting for the CTN value and slope measured here, we find an overall decrease in the expected Advanced LIGO binary neutron star range of 7% (from 186 Mpc to 171 Mpc [24]) compared to [22, 23], see figure 4.

D. Loss angle of $\text{TiO}_2:\text{Ta}_2\text{O}_5$

To estimate the loss angle for the titania-tantala alloy used as the high refractive index material in the Advanced LIGO coatings, we use the equations given in [25] and assume a loss angle for silicon-dioxide (the low index material) of $\phi_{\text{SiO}_2} = 5 \times 10^{-5}$ [26]. We further assume that the loss angles associated with shear and bulk deformation are equal in both coating materials. We have moved away from the simplified CTN equations from [20] used in our previous publication because that calculation neglects field penetration into the coating and thus underestimates the loss angle of the high index material by 4%. The current experiment's precision is sufficient to make this a non-negligible effect.

Our estimate for the loss angle of the high-refractive-index material in the Advanced LIGO coatings is

$$\phi_{\text{Ti:Ta}} = (3.6 \pm 0.1) \times 10^{-4} \left(\frac{f}{100 \text{ Hz}} \right)^{0.1 \pm 0.04} \quad (12)$$

This number is slightly lower than the value previously

reported in [26], but higher than the values reported in [15, 27].

Using the same procedure, we estimate the loss angle of tantalum in the $\text{Ta}_2\text{O}_5\text{-SiO}_2$ coatings. We obtain the same value for both coatings,

$$\phi_{\text{Ta}} = (5.3 \pm 0.1) \times 10^{-4} \left(\frac{f}{100 \text{ Hz}} \right)^{0.06 \pm 0.02}, \quad (13)$$

which is higher than reported in [28, 29].

VI. CONCLUSIONS

Precision measurements of coating thermal noise are critical to determining the future of both high-precision laboratory-scale R&D, and large scale efforts such as gravitational-wave detectors. Our finding that the CTN spectrum does not follow the expected slope will allow for more reliable computations of CTN from measurements of the mechanical properties, and more accurate extrapolations of direct CTN measurements to other frequency bands.

For Advanced LIGO in particular, the measurements presented herein allow us to update our understanding of the sensitivity achievable by current detectors. The spectrum of CTN estimated for Advanced LIGO from measurements presented in this work is higher than the one originally computed for Advanced LIGO, resulting in a 7% reduction in the detectors' expected range. Similar impacts are expected for other gravitational-wave detectors, and both the amplitude and slope of CTN measured here will need to be incorporated into future detector designs.

ACKNOWLEDGMENTS

The authors would like to acknowledge the unfailing support and recognition of the LIGO Scientific Collaboration's optics working group without which this work would not have been possible. We are also very grateful for the computing support provided by The MathWorks, Inc.

LIGO was constructed by the California Institute of Technology and Massachusetts Institute of Technology with funding from the National Science Foundation, and operates under cooperative agreement PHY-0757058. Advanced LIGO was built under award PHY-0823459. This paper carries LIGO Document Number LIGO-P1700448.

-
- [1] G. M. Harry *et al.*, *Classical and Quantum Gravity* **24**, 405 (2007).
- [2] M. Evans, S. Ballmer, M. Fejer, P. Fritschel, G. Harry, and G. Ogin, *Phys. Rev. D* **78**, 102003 (2008).
- [3] A. D. Ludlow, X. Huang, M. Notcutt, T. Zanon-Willette, S. M. Foreman, M. M. Boyd, S. Blatt, and J. Ye, *Opt. Lett.* **32**, 641 (2007).
- [4] T. Kessler, C. Hagemann, C. Grebing, L. Legero, U. Sterr, F. Riehle, M. J. Martin, L. Chen, and Y. J., *Nature Photonics* **6**, 687 (2012).
- [5] B. Abbott *et al.*, *New Journal of Physics* **11**, 073032 (2009).
- [6] M. Poot and H. S. van der Zant, *Physics Reports* **511**, 273 (2012), mechanical systems in the quantum regime.
- [7] G. D. Cole, W. Zhang, B. J. Bjork, D. Follman, P. Heu, C. Deutsch, L. Sonderhouse, J. Robinson, C. Franz, A. Alexandrovski, M. Notcutt, O. H. Heckl, J. Ye, and M. Aspelmeyer, *Optica* **3**, 647 (2016).
- [8] The LIGO Scientific Collaboration and J. Harms, *Classical and Quantum Gravity* **34**, 044001 (2017).
- [9] J. Miller, L. Barsotti, S. Vitale, P. Fritschel, M. Evans, and D. Sigg, *Phys. Rev. D* **91**, 062005 (2015).
- [10] M. Punturo *et al.*, *Classical and Quantum Gravity* **27**, 194002 (2010).
- [11] D. R. M. Crooks, P. Sneddon, G. Cagnoli, J. Hough, S. Rowan, M. M. Fejer, E. Gustafson, R. Route, N. Nakagawa, D. Coyne, G. M. Harry, and A. M. Gretarsson, *Classical and Quantum Gravity* **19**, 883 (2002).
- [12] G. M. Harry, A. M. Gretarsson, P. R. Saulson, S. E. Kittelberger, S. D. Penn, W. J. Startin, S. Rowan, M. M. Fejer, D. R. M. Crooks, G. Cagnoli, J. Hough, and N. Nakagawa, *Classical and Quantum Gravity* **19**, 897 (2002).
- [13] V. Pierro and I. M. Pinto, *Measuring Coating Mechanical Quality Factors in a Layered Cantilever Geometry: a Fully Analytic Model*, Tech. Rep. (TWG, University of Sannio at Benevento, 2006).
- [14] E. Cesarini, M. Lorenzini, E. Campagna, F. Martelli, F. Piergiovanni, F. Vetrano, G. Losurdo, and G. Cagnoli, *Review of Scientific Instruments* **80**, 053904 (2009).
- [15] S. Gras, H. Yu, W. Yam, D. Martynov, and M. Evans, *Phys. Rev. D* **95**, 022001 (2017).
- [16] The LIGO Scientific Collaboration, *Classical and Quantum Gravity* **32**, 074001 (2015).
- [17] R. Kubo, *Reports on Progress in Physics* **29**, 255 (1966).
- [18] Y. Levin, *Phys. Rev. D* **57**, 659 (1998).
- [19] V. Braginsky, M. Gorodetsky, and S. Vyatchanin, *Physics Letters A* **264**, 1 (1999).
- [20] W. Yam, S. Gras, and M. Evans, *Phys. Rev. D* **91**, 042002 (2015).
- [21] A. Siegman, *Lasers* (University Science Books, 1986).
- [22] D. V. Martynov *et al.*, *Phys. Rev. D* **93**, 112004 (2016).
- [23] J. Aasi *et al.*, *Classical and Quantum Gravity* **32**, 074001 (2015).
- [24] H.-Y. Chen, D. E. Holz, J. Miller, M. Evans, S. Vitale, and J. Creighton, (2017), arXiv:1709.08079.
- [25] T. Hong, H. Yang, E. K. Gustafson, R. X. Adhikari, and Y. Chen, *Phys. Rev. D* **87**, 082001 (2013).
- [26] M. Principe, I. M. Pinto, V. Pierro, R. DeSalvo, I. Taurasi, A. E. Villar, E. D. Black, K. G. Libbrecht, C. Michel, N. Morgado, and L. Pinard, *Phys. Rev. D* **91**, 022005 (2015).
- [27] R. Flaminio, J. Franc, C. Michel, N. Morgado, L. Pinard, and B. Sassolas, *Classical and Quantum Gravity* **27**, 084030 (2010).
- [28] S. D. Penn, P. H. Sneddon, H. Armandula, J. C. Betzwieser, G. Cagnoli, J. Camp, D. R. M. Crooks, M. M. Fejer, A. M. Gretarsson, G. M. Harry, J. Hough, S. E. Kittelberger, M. J. Mortonson, R. Route, S. Rowan, and C. C. Vassiliou, *Classical and Quantum Gravity* **20**, 2917 (2003).
- [29] D. R. M. Crooks, G. Cagnoli, M. M. Fejer, G. Harry, J. Hough, B. T. Khuri-Yakub, S. Penn, R. Route, S. Rowan, P. H. Sneddon, I. O. Wygant, and G. G. Yaralioglu, *Classical and Quantum Gravity* **23**, 4953 (2006).